Continuum-discontinuum simulation of effects of internal friction angle on local fracture of circular cavern surrounding rock under hydrostatic pressure

Xue-yuan BAI
College of Mechanics and Engineering, Liaoning Technical University, Fuxin, Liaoning 123000, China

Xue-bin WANG
Institute of Computational Mechanics, Liaoning Technical University, Fuxin, Liaoning 123000, China

Qin SHU
College of Mechanics and Engineering, Liaoning Technical University, Fuxin, Liaoning 123000, China

Custom Citation
BAI Xue-yuan, WANG Xue-bin, SHU Qin, . Continuum-discontinuum simulation of effects of internal friction angle on local fracture of circular cavern surrounding rock under hydrostatic pressure[J]. Rock and Soil Mechanics, 2020, 41(7): 2485-2493.

Continuum-discontinuum simulation of effects of internal friction angle on local fracture of circular cavern surrounding rock under hydrostatic pressure

BAI Xue-yuan[1],　WANG Xue-bin[1, 2],　SHU Qin[1]

1. College of Mechanics and Engineering, Liaoning Technical University, Fuxin, Liaoning 123000, China

2. Institute of Computational Mechanics, Liaoning Technical University, Fuxin, Liaoning 123000, China

Abstract: In order to simulate the transition of rock from continua to discontinua more accurately and reduce the mesh dependence, an element splitting method is developed based on the continuum-discontinuum method where the Lagrangian element method is coupled with discrete element method. The computational domain is discretized into high-precision quadrilateral elements; after cracking, the cracks can propagate along the diagonal lines of quadrilateral elements and the edges of triangular or quadrilateral elements. Deformation-cracking processes of the Brazilian disc rock specimen, uniaxial compression rock specimen and surrounding rocks under hydrostatic pressure are simulated. The following results are found. (1) For the Brazilian disc rock specimen, tensile cracks propagate from the center of the disc to the top and bottom until they penetrate through the disc, and the tensile cracks are relatively smooth; for the uniaxial compression rock specimen, shear cracks are relatively straight, and the direction of the main shear crack penetrating through the rock specimen is consistent with the shear plane direction obtained according to the Mohr-Coulomb criterion. (2) From the effects of hydrostatic pressure and internal friction angle on deformation-cracking processes, the following results are found. Under hydrostatic pressure, firstly, V-shaped notches appear near the cavern surface due to shear crack propagation; then, long and curved shear cracks appear due to further shear crack propagation whose distribution is similar to shear slip-lines. With an increase of hydrostatic pressure, the ranges of shear cracks increase, whereas with an increase of internal friction angle, the ranges of shear cracks decrease, and the angle between the propagation direction of the long shear crack and the annular direction decreases. (3) According to the simulation of the surrounding rock in phase-Ⅱ Tianshengqiao hydropower station, four V-shaped notches are observed, which is in a good agreement with field observation.

Keywords: mesh dependence; cavern surrounding rock; deformation-cracking process; hydrostatic pressure; internal friction angle; shear slip-line

1 Introduction

Subjected to high in-situ stress, rock burst and other disasters are tend to occur during cavern excavation. For instance, in the "11.28" accident of Jinping Hydropower Station in 2009, a massive rock burst occurred in the drainage tunnel, resulting in seven deaths and one injury. Tianshengqiao Hydropower Station has also suffered from rock bursts many times.

The test and field observations indicate that the surrounding strata often shows the characteristics of local fracturing, which can be divided into tensile failure and shear failure according to the failure mechanism. Specifically, tensile failure can be further divided into near-field tensile failure and far-field tensile failure. Both of them generally occur when the difference between the minimum principal stress and the maximum principal stress is relatively large. Shear failure can be subdivided into V-shaped notch and narrow shear crack. Two principal stresses that differ significantly, or are approximately equal to each other, are the prerequisites for V-shaped

notch occurring in hard surrounding rocks. For example, when the difference between σ_1 and σ_3 is large, the tips of the two V-shape notches are aligned in the direction of σ_3; when two principal stresses are approximately equal, V-shaped notches appear at four symmetrical positions at 45° along with the directions of σ_1 and σ_3. Narrow shear cracks are generally triggered on the basis of V-shaped notches. Compared with V-shaped notches, the conditions for the formation of narrow shear cracks are as follows: the difference between σ_1 and σ_3 is further increased, the difference between σ_1 and σ_3 is close to or equal to 0, and the lithology of the surrounding rock is soft in hardness. For instance, when σ_1 differs greatly from σ_3, the long axis of the elliptic envelope of the narrow shear crack is along the direction of σ_3; when σ_1 is close to or equal to σ_3, shear cracks appear around the cavern. Figure 1(a) shows the results of sandstone model and similar material under hydrostatic pressure when the difference between σ_1 and σ_3 remains constant[2–3]. Figure 1(b) demonstrates the field observations[4].

Figure 1(c) illustrates the results of sandstone model and similar material model under hydrostatic pressure, respectively.

(a) Test results of V-shape notch [2–3]   (b) Field results of slip-lines [4]

(c) Test results of slip-lines [5–6]   (d) Theoretical results of slip-lines [7]
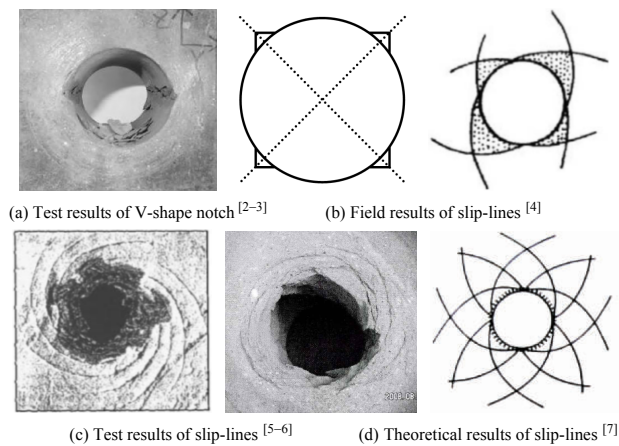
Fig. 1 Common failure modes of surrounding rocks

In theoretical studies, although slip-lines[7] can be obtained according to plasticity theory (see Fig. 1(d)), their spacing and quantity cannot be quantified. In contrast, the failure process of surrounding rock can be simulated by numerical method. Common numerical simulation methods include continuous and discontinuous methods. In literature [8], the finite element method has been adopted to predict the annular plastic zone distribution of the surrounding rock of the circular cavern under hydrostatic pressure[8]. However, although continuous method is able to simulate the distribution of plastic zone, it is difficult to simulate discontinuous phenomena such as block shedding, sliding and ejection[9]. By introducing strength criteria and virtual fracture model, discontinuous method is capable to simulate the failure of surrounding rock, but it usually needs to cooperate with normal or tangential stiffness, which will affect the stress and strain calculation of continuous media.

In order to make up the deficiency of continuous and discontinuous methods, scientists have developed some continuous-discontinuous methods[10–12], such as the finite element and discrete element coupling method. Literature [13] developed an adaptive analysis method of local element splitting based on continuous-discontinuous method. The cracks can extend along the boundary and middle line of triangular element, reducing the dependence of grid itself. In literature [14], contact forces between elements are solved by using the potential contact force calculation based on an unified calibration, which solves the problem of the deviation of contact force under the same embedding quantity. At present, these methods have been applied to study the failure process of surrounding rocks[15–17]. For example, literature [15] used the coupling method of finite element and discrete element to simulate the

failure process of surrounding rock induced by excavation. In literature [17], a continuous-discontinuous method in which Lagrange element coupled with discrete elements was used to simulate the collapse process of surrounding rock under displacement controlled loading. This method discretizes the model into many quadrilateral elements and introduces strength criteria and virtual fracture model to simulate the fracture extension. The shear slip-lines or shear surfaces obtained by tests and plasticity theory are smooth and curved (Fig. 1(c)–1(d)). It is well known that the direction of shear plane based on Mohr-Coulomb criteria is related to the internal friction angle of the rock. With regard to rock under hydrostatic pressure, the change of the internal friction angle will change the shape of the curved shear plane. However, the above phenomena cannot be simulated by using the continuous-discontinuous method[17], in which the fracture only propagate along the boundary of the quadrilateral element.

In order to more accurately simulate the transition of rock from continuous medium to discontinuous medium, a new method that quadrilateral elements can split diagonally is proposed based on the self-developed continuous-discontinuous method[11, 17]. The deformation and failure processes of Brazilian disk rock sample, uniaxial compression rock sample and the surrounding rock of cavern under hydrostatic pressure are modeled, and the influence of hydrostatic pressure and internal friction angle on local fracture characteristics are explored in detail.

2 Continuous-discontinuous method considering diagonal cracking

2.1 Methodology

Before cracking, the quadrilateral elements with high calculation accuracy are adopted. After cracking, the created cracks can propagate along the boundary of the element or split the quadrilateral element along the diagonal line. Compared with the previous cracking method that the fracture can only extend along the element boundary[11,17], there are more fracture extension paths for new cracking method. In addition, only one element is added when diagonal cracking occurs, the computation only increases slightly, and the time step length does not decrease. Therefore, the computational efficiency is enhanced substantially.

The possible cracking paths of the previous method and the present method are illustrated in Fig. 2. Assume that the crack tip is located at node A. For previous method, cracks can only extend along the boundary of quadrilateral elements, and thus there are only 4 possible cracking paths (dashed line in Fig. 2(a)). For new method, cracks can extend along element boundaries or split quadrilateral elements diagonally. As a consequence, there are 7 possible crack paths (dashed line in Fig. 2(b)).
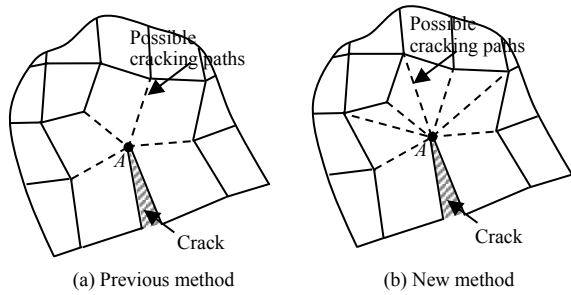
Fig. 2 Schematic of possible cracking paths of the previous method and the new method

2.2 Computation procedure

The Computation procedure of continuous-continuous method considering diagonal cracking is as follows:

(1) At each time step, the strain increment of the element can be obtained according to the information of each node (position and velocity), and then the stress increment of the element can be calculated by the generalized Hooke's Law.

(2) Judge whether the stress of each node (obtained by the stress of all elements around the node according to areal weighted average) meets the failure criteria. If so, split the node into two. And then judge whether tension or shear failure occurs. It is unnecessary to judge whether shear fracture will occur if tension failure criteria is met first. The tensile crack criteria can be expressed as

$$\sigma_t - \sigma_3 \leqslant 0 \tag{1}$$

where σ_3 is the maximum principle stress; σ_t is the uniaxial tensile strength. Shear failure criteria can be formulated by

$$\sigma_1 - \sigma_3 \frac{1+\sin\varphi}{1-\sin\varphi} + 2c\sqrt{\frac{1+\sin\varphi}{1-\sin\varphi}} \leqslant 0 \tag{2}$$

where σ_1 is the minimum principle stress; c is the cohesion; and φ is the internal friction angle.

If the node stress meets the failure criteria, calculate the angle between the possible cracking paths (all elements' boundaries and the diagonals of quadrilateral elements) and the theoretical cracking direction. Among the possible cracking paths, choose the one with the smallest angle to the theoretical cracking direction as the actual cracking direction. If the angle between the diagonal of the quadrilateral element and theoretical cracking direction is the smallest, it will crack along the diagonal.

Take the cracking along the diagonal as an example. If the node stress meets the failure criteria and the newly formed crack extends along the diagonal of the quadrilateral element, then the element will be split into two elements. For quadrilateral element $ABCD$ (Fig. 3(a)), if node A meets the failure criteria, node A will be separated into A' and A'' (Fig. 3(b)), and their

initial information (position and velocity, etc.) will be inherited from node A. In this way, the quadrilateral element $ABCD$ splits into two triangular elements $A''BC$ and $A'CD$, and their initial stress states are inherited from the quadrilateral element $ABCD$. Consequently, a fracture zone is formed during this process. (Fig. 3(b)). If the stresses of two nodes in a quadrilateral element satisfy the cracking criteria simultaneously, and the cracking direction of the two nodes is along the diagonal of the quadrilateral element, due to the mutual influence of the cracking of the two nodes, after the cracking along the diagonal, the quadrilateral element is divided into two triangles. In the actual processing, considering that there is a certain sequence of node numbering, the diagonal cracking of the element with small number nodes are allowed to form two triangular elements. Since the quadrilateral is divided into two triangles, the nodes with large numbers can only cracking along one boundary of the triangle element.

(a) Before element cracking   (b) After cracking along the diagonal of the element
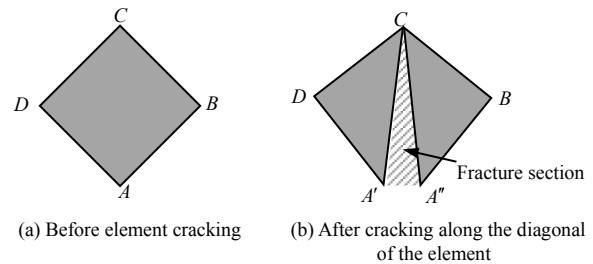
Fig. 3 Schematic of element internal cracking

The softening of rock was simulated by applying normal and tangential cohesion forces on fracture sections. The normal cohesion decreases linearly with the increase of normal opening degree of the fracture sections. With the increase of tangential slip, the tangential cohesion decreases linearly. It should be noted that the fracture sections which meet the tensile failure criteria and the shear fracture criteria are the tensile fracture section and the shear fracture section, respectively.

(3) A contact retrieval method based on spatial partition is used to obtain the contact relationship between each element. The contact force calculation method based on potential function[18] is adopted to solve the contact force. At present, the potential functions are mostly developed based on the triangle element. The shortest distance from the embedding point to each side of a triangular element can be simply extended to the shortest distance from each side of the quadrilateral element, so that the potential function based on the quadrilateral element can be established.

(4) According to a variety of forces (elastic forces and external forces, etc.) and the mass of the node, the node velocity can be calculated using Newton's second Law and the central difference method, and then the displacement of the node can be obtained.

3 Method validation

3.1 Simulation of deformation-cracking process of Brazilian disk sample

The diameter and thickness of the Brazilian disk rock specimen are 0.05 m and 0.025 m, respectively. The rock sample (fine sandstone) is of standard size and is divided into 2 355 quadrilateral elements, which are loaded by a loading plate. The lower loading plate is fixed, and the downward moving velocity *v* of the upper loading plate is 0.1 m/s (Fig.4(a)). It should be noted that the loading velocity adopted by the indoor quasi-static test is less than the value used in this study. Through numerical study, the literature[19] found that the numerical results have little difference when the

loading rate was less than 0.25 m/s. The time step is 3.080 98×10⁻⁸ s, and the gravitational acceleration is 10 m/s². Other physical and mechanical parameters are listed in Table 1. The calculation is carried out under the conditions of plane strain and large deformation.

The above mechanical parameters include macroscopic parameters (elastic modulus, Poisson's ratio, tensile strength, cohesion, and internal friction angle) and mesoscopic parameters (fracture energy and normal contact stiffness). For macroscopic parameters, the measured values can be directly used for simulation. As for the mesoscopic parameters, the empirical selections can be used for trial calculation until it is consistent with the actual results.

Table 1 Physical and mechanical parameters

Model	Areal density /(kg · m⁻²)	Elastic modulus /GPa	Poisson's ratio	Tensile strength /MPa	Cohesion /MPa	Internal friction angle /(°)	Type Ⅰ fracture energy /(N · m⁻¹)	Type Ⅱ fracture energy /(N · m⁻¹)	Locally adaptive damping coefficient	Friction coefficient	Normal contact stiffness /GPa
Brazilian disc	2 220	3	0.27	2.15	15	25	20	100	0.2	0.1	130
uniaxial compression rock	2 430	11.4	0.27	5	12.9	25	20	100	0.2	0.1	400

(a) Mechanical model

(b) Number of time step =100 000

(c) Number of time step=195 000

(d) Number of time step =210 000

(e) Number of time step =250 000

(f) Load−displacement curves
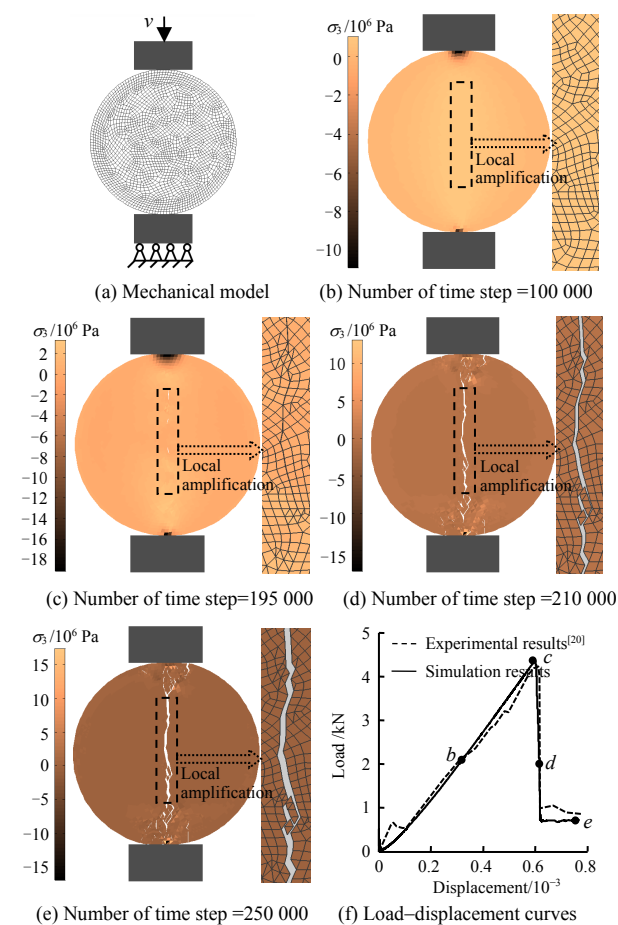
Fig. 4 Mechanical model, spatiotemporal distributions of σ_3 and load-displacement curves of the Brazilian disc

Figure 4 shows the mechanical model, spatial and temporal distribution, and the simulated and measured results of the load-displacement curve of the Brazilian

disk rock. A positive value of σ_3 represents tension, whereas a negative value of σ_3 represents compression. The points *b−e* in Fig. 4(f) correspond to Figs.4(b)− 4(e) respectively. The right parts of Figs. 4(b)−4(e) are local amplification of the areas between the upper and lower parts of the sample, which reflect fracture features in detail. It can be found that, before cracking, the higher σ_3 region shows an upright spindle shape, and there is a stress concentration zone near the upper and lower end of the disc (Fig. 4(b)). Then the tensile crack propagates from the center of the disc upward and downward (Fig. 4(c)) until it penetrates the disc sample (see Figs. 4(d)−4(e)).

The observed results in this paper are superior to those in the literature [11]. The cracks in our study are more straight and fewer in number, which is more consistent with the experimental results, while the cracks in literature [11] are more irregular and have a zonal distribution.

When the cracks start to extend from the center of the Brazilian disc rock, the measured uniaxial tensile strength is written as

$$\sigma_t = \frac{2P}{\pi DL} \tag{3}$$

where *D* and *L* are the diameter and thickness of the disc, respectively; and *P* is the measured peak load. From Fig. 4(f), it can be found that *P* is 4.37 kN. By substituting *P* into Eq. (3), the actual measured σ_t is 2.22 MPa, which is close to the value adopted in the calculation (2.15 MPa). More importantly, the numerical results of the load−displacement curve are in good agreement with the test results[20].

3.2 Simulation of deformation-cracking process of uniaxial compression sample

The uniaxial compression rock sample is sandy mudstone. The size is 0.05 m×0.1 m, and is divided into 100×200 square elements. The lower boundary of the rock sample is constrained by fixed hinge supports, while the upper boundary is constrained by horizontal hinge supports. The downward movement velocity of the upper boundary is 0.15 m/s (Fig. 5(a)). The time step is $5.16274×10^{-8}$s, and the gravitational acceleration is 9.8 m/s². Other physical and mechanical parameters are listed in Table 1. The calculation is carried out under the conditions of plane strain and large deformation.

Figures 5(b)−5(f) shows the spatial and temporal distribution and stress−strain curve of the sample. The white and black lines in the nephograms represent tensile fracture section and shear fracture section respectively. Multiple fracture sections are connected together to form cracks. Points *b−e* in Fig. 5(f) correspond to 5(b)−5(e), respectively. It can be found that before cracking, stress (σ_1) concentration occurs at the four corners of the sample (Fig. 5(b)); after cracking, the two shear fractures extend from the two apex angles of the upper end face to the interior obliquely and are intersected (Figs. 5(c)−5(d)) until a main shear crack penetrates the rock sample (Fig. 5(e)).

(a) Mechanical model　(b) Number of time step=20 000　(c) Number of time step=31 600

(d) Number of time step=32 000　(e) Number of time step =33 600　(f) Stress-strain curve
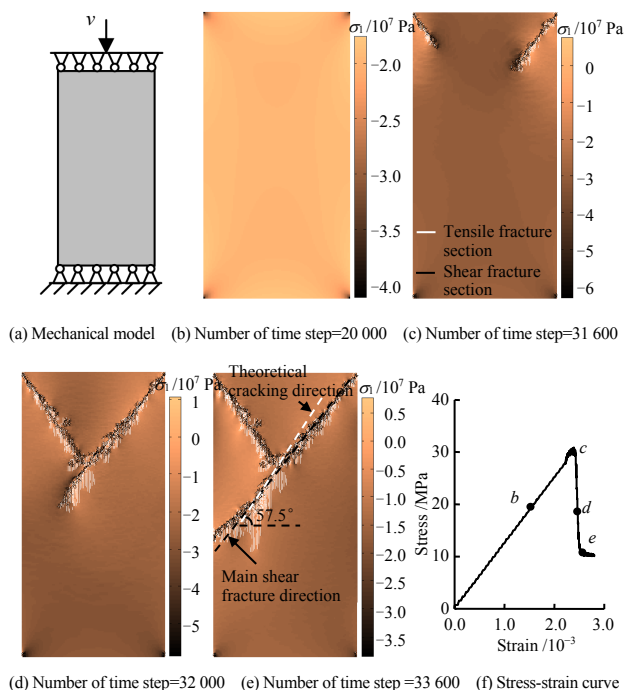
Fig. 5　Mechanical model, spatiotemporal distributions of σ_1 and the stress−strain curve of the uniaxial compressive rock specimen

For this uniaxial compression sample, the angle between the shear failure plane based on the Mohr‒Coulomb criteria (white dashed line in Fig. 5(e)) and the horizontal direction is $45°+\varphi/2$, that is 57.5°. The

angle between the main shear fracture (black dashed line in Fig. 5(e)) and the horizontal direction is about 55°. The difference between these two angles is insignificant.

4　Simulation of deformation-cracking process of cavern surrounding rock

4.1 Model and parameters

The size of the model is 40 m×40 m and the lithology is sandy mudstone. Before excavation, the model is divided into 160×160 square elements with transmission boundary around. The calculation is carried out under the conditions of plane strain and large deformation.

Physical and mechanical parameters are as follows: surface density is 2 430 kg/m²; elastic modulus is 17.4 GPa; Poisson's ratio is 0.27; uniaxial tensile strength is 5 MPa; cohesion is 8.5 MPa; type Ⅰ and type Ⅱ fracture energy are 20 N/m and 100 N/m, respectively; local adaptive damping coefficient is chosen as 0.2; friction coefficient is 0.1; normal contact stiffness is 200 GPa; and time step is set as $2.089 43×10^{-5}$ s. Gravity is not taken into account in the model.

4.2 Calculation process and scenarios

Step 1: Under the influence of hydrostatic pressure *p*, the unexcavated model reaches static equilibrium with a total of 2000 time steps.

Step 2: A cavern with a diameter of 6 m is excavated in the center of the model. The excavation is simulated by removing the corresponding elements. The excavation is carried out in three times and the elements within the radius of 1, 2 and 3 m are deleted successively. The excavation interval is 500 time steps, during which process hydrostatic pressure remains unchanged.

Step 3: Keep *p* constant, calculate the failure process of the surrounding rock after excavation.

A total of 7 simulation scenarios are conducted. Internal friction angle of scenarios 1 to 4 are 25° and hydrostatic pressure are 30, 40, 50 and 60 MPa, respectively. Scenarios 5 to 7 have a same hydrostatic pressure, 50 MPa, and different internal friction angles (15°, 20° and 30°). Scenarios 1 to 4 aims to study the influence of hydrostatic pressure, while scenarios 3, 5 to 7 are designed to study the impact of internal friction angle.

The vertical stress (approximately equal to annular stress) and horizontal stress (approximately equal to radial stress) of all elements at the horizontal symmetry lines of the left half of the rock after excavation are monitored.

4.3 Influence of hydrostatic pressure

Figure 6 displays the spatial and temporal distribution of the fractures and σ_1 in scenario 3. The white and black line represent tensile fracture sections and shear fracture sections, respectively. Multiple fracture sections are connected together forming cracks. Figure 7 records the vertical stress and horizontal stress of the monitoring

(a) Number of time step =3 000 (b) Number of time step =3 500 (c) Number of time step =4 000 (d) Number of time step =4 500

(e) Number of time step =5 000 (f) Number of time step =6 000 (g) Number of time step =8 000 (h) Number of time step =11 000

Fig. 6 Spatiotemporal distributions of cracks and σ_1 of scheme 3

(a) Vertical stress

(b) Horizontal stress
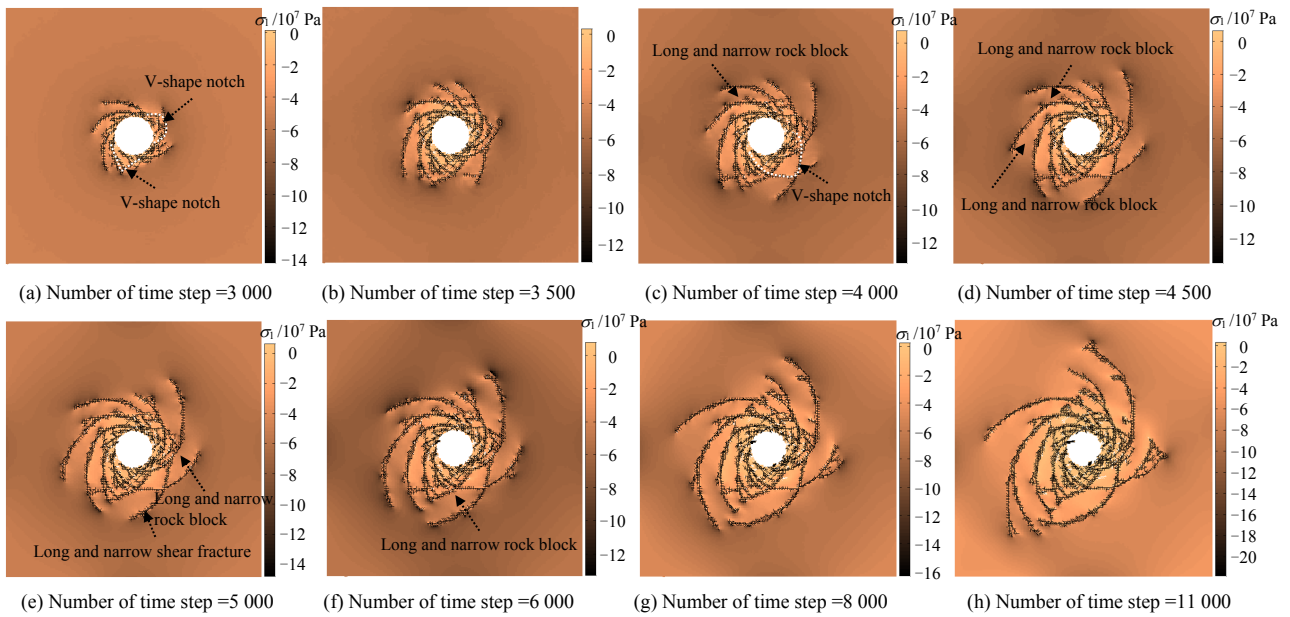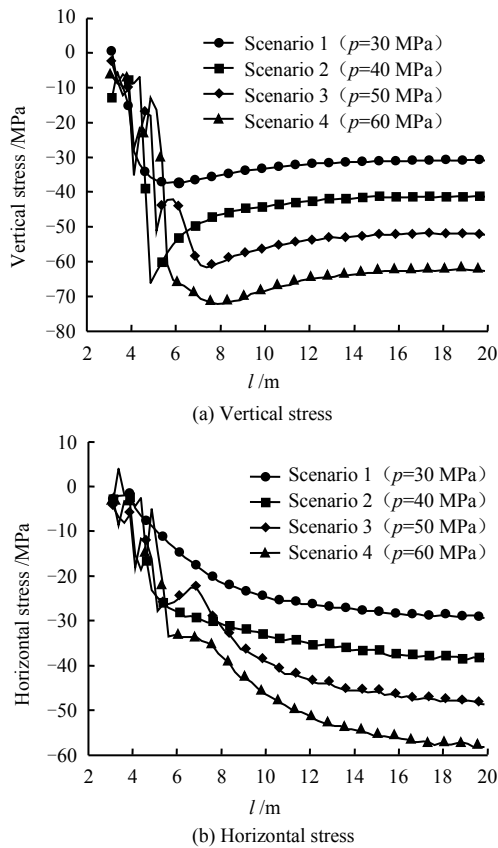
Fig. 7 Evolution of stresses of monitored elements with l of scenarios 1−4

element after excavation (time steps is 3000). The x-coordinate l is the distance between the centroids of the cavern and monitoring element. In Fig.8, the number of shear fracture sections are plotted against the time steps in scenarios 1 to 4 after excavation. Figure 9 shows the distribution of fractures and σ_1 in scenarios 1 to 4 when the time steps is 5000.

It can be seen from Fig. 6 that the surrounding rock

has fractured locally. When the excavation is completed, several curved shear fractures extending counterclockwise have formed near the cavern surface, and they are intersected with a few clockwise shear fractures, forming V-shaped notches (Fig. 6(a)). Similar to the shear slip-line, with the increase of time steps, the length of shear fracture increases gradually. Furthermore, the number of V-shape notch also increases. The surrounding rock near the cavern surface are fragmented, while the surrounding rock are elongated and blocky inside the cavern (Figs. 6(b)−6(h)). Tensile fractures are mostly distributed near the cavern surface and a small number of tensile fractures in the surrounding rock are generated along with the shear fractures. The propagation speed of shear fractures toward the interior of the rock witnesses a downward trend. For example, when the number of time steps increases from 3000 to 5000, the maximum distance between the shear fractures and cavern surface increases by about 5.2 m, while when time steps increases from 6000 to 8000, such a distance increases by about 1.8 m.
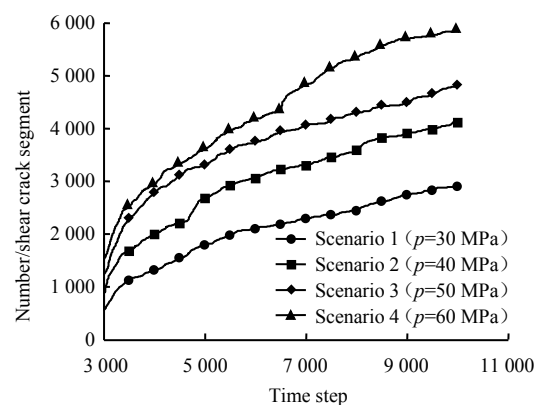
Fig. 8 Evolution of the number of shear crack segments with time steps of scenarios 1−4

(a) Scenario 1（p=30 MPa）   (b) Scenario 2（p=40 MPa）   (c) Scenario 3（p=50 MPa）   (d) Scenario 4（p=60 MPa）
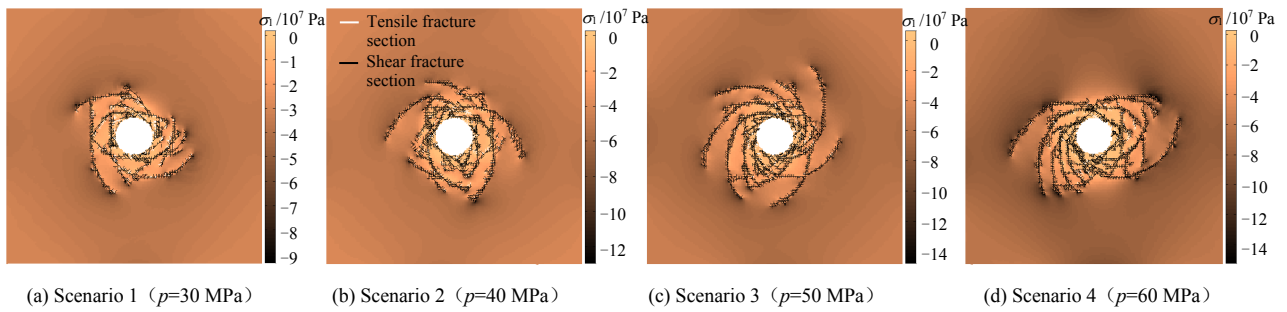
Fig. 9 Distributions of cracks and σ_1 of scenarios 1−4 (timestep is 5 000)

After excavation, the radial stress of surrounding rock near cavern surface decreases. The stress state, from inside to outside, changes from bidirectional compression to nearly unidirectional compression. When the failure criteria is met, the surrounding rock will undergo shear and tensile fracture along with the stress transferring inwardly. The extension directions of shear fractures are similar to the radial angles, indicating that the bending degree of narrow shear fractures formed by each shear fracture are similar, which is analogous to shear slip-lines.

Literature [7] obtained a regular slip-line network through plasticity theory (Fig. 1(d)). In fact, there are interactions between multiple fractures (after the shear fractures crosses, the extension of one shear fracture may be dominant, thus hindering the propagation of another shear fracture (Fig. 5(e)). This accounts for the irregular distribution of shear fractures obtained in this study (Fig. 6). Similar results were documented in literature [5], in which the failure process of sandstone samples containing circular caverns under hydrostatic pressure was studied. The shear fractures near the cavern surface are relatively dense, while the shear fractures inside the surrounding rocks are relatively sparse. From near to far, the failure mode of surrounding rock transfers from fragments to long and narrow blocks.

Figure 7 shows that for a smaller l, both the vertical stress−l curve and the horizontal stress−l curve of the monitoring element are not smooth since the monitoring element is close to the fracture. However, for a larger l, with the increase of l, the vertical stress of the monitoring element increases first and then decreases, while the horizontal stress keeps increasing. The vertical stress and horizontal stress of the monitoring element near the boundary of surrounding rock approaches p. With the increase of p, the vertical and horizontal stress of the monitoring unit that is far away from the fracture goes up.

It can be seen from Fig. 8 that after excavation, with the increase of the number of time steps, the growth rate of the quantity of shear fracture sections increases from fast to basically unchanged or slightly declined. Under the same number of time steps, the number of shear fracture sections increases with the increase of p. For example, when the number of time steps is equal to 5000, the number of shear fracture sections in scenarios 1 to 4 is about 1800, 2660, 3300 and 3620, respectively.

From Fig. 9, it is clear that under the same number of time steps, with the increase of p, the maximum depth of shear fracture extending to the interior of surrounding rock tends to increase, which is in accordance with the rules reflected in Fig. 8.

4.4 Influence of internal friction angle

Figure 10 illustrates the spatial and temporal distribution of the fractures and σ_1 in scenario 6. In Fig. 11, the number of shear fracture sections and time-step number curves in scenarios 3, 5−7 are plotted. Figure 12 shows the detailed distribution of shear fractures and σ_1 in scenarios 3, 5−7 when the number of time steps is 5000.

It can be seen from Fig. 10 that the narrow shear fractures in scenario 6 mostly extend counterclockwise. For a given number of time steps, the length difference among each narrow shear fractures are insignificant.

In Fig. 11, with the increase of the number of time steps, the number of shear fracture sections experiences a remarkable rise, and then remains almost unchanged.

Figure 12 reveals that when the number of time steps is 5000, the maximum depth of shear fracture extending to the interior of surrounding rock decreases with the increase of φ. This is because a larger φ leads to a higher shear strength of the rock, and the more difficult it is for shear fractures to extend. In addition, the smaller the angle between the fracture extension direction and the cavern annular direction, (the more curved the narrow shear fractures), the smaller the spacing between adjacent narrow shear fractures. Under the same number of time steps, the number of shear fracture sections decreases with the increase of φ, which is consistent with the rules reflected in Fig. 11.

In practice, it is difficult to prevent shear fracture of surrounding rock at the initial stage of excavation. Therefore, the key of reinforcement of surrounding rock is to prevent further shear failure and slip. The smaller the internal friction angle, the higher the reinforcement strength is demanded.

(a) Number of time step =3 000

(b) Number of time step =3 500

(c) Number of time step =4 000

(d) Number of time step =4 500

(e) Number of time step =5 000

(f) Number of time step =6 000

(g) Number of time step =7 000

(h) Number of time step =9 000
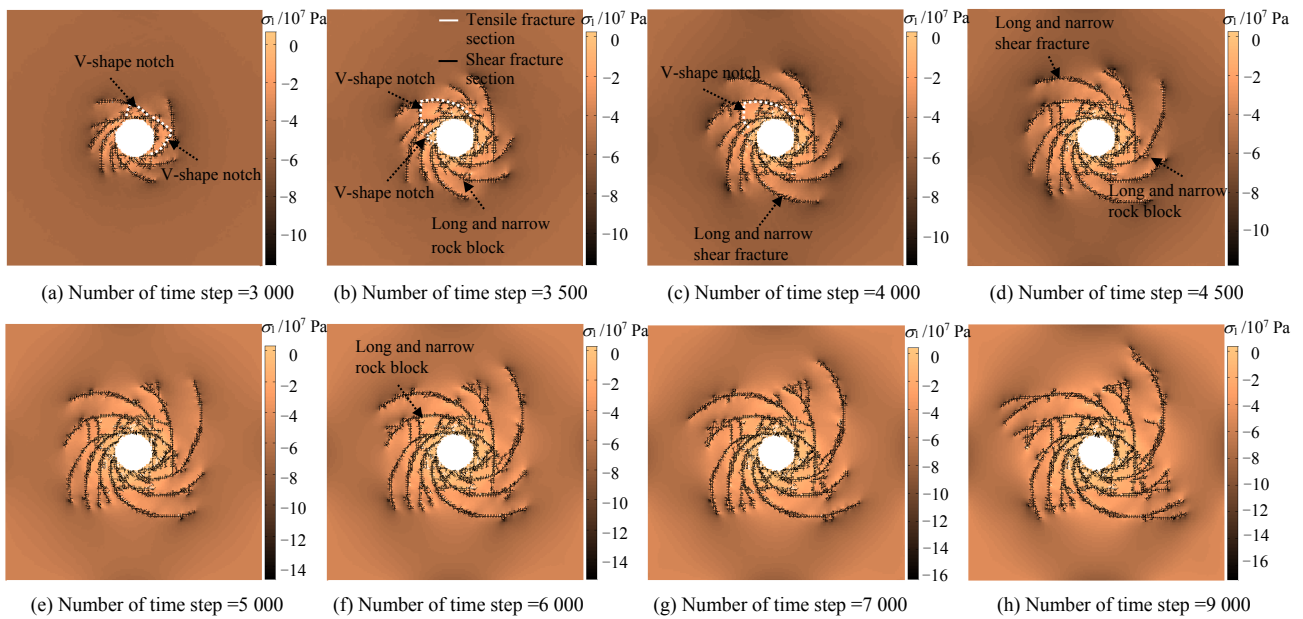
Fig. 10   Spatiotemporal distributions of cracks and σ_1 of scenario 6
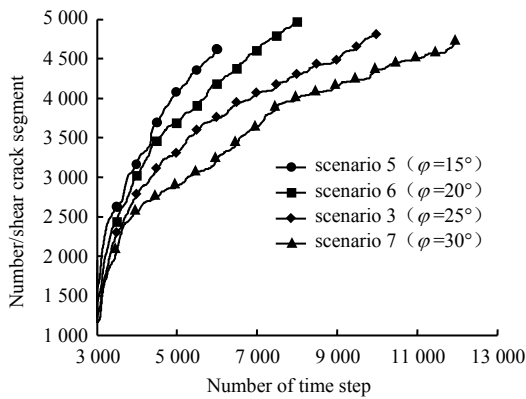
**Fig. 11   Evolution of the number of shear crack segments
with timesteps of scenarios 3 and 5-7**

(a) scenario 5（φ=15°）

(b) scenario 6（φ=20°）

(c) scenario 3（φ=25°）

(d) scenario 7（φ=30°）
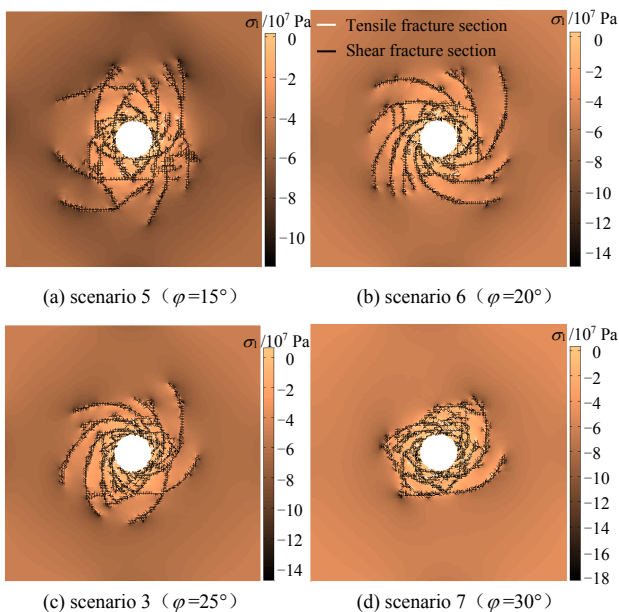
**Fig. 12   Distributions of cracks and σ_1 of scenarios 3 and
5-7 (timestep is 5 000)**

5   Engineering case analysis

5.1 Model, parameters and calculation procedure

The circular cavern of Tianshengqiao Hydropower Station Ⅱ is 9.5−10.8 m in diameter and buried at a depth of 400−700 m. Section 5+470−500 of No. 2 main cavern is under hydrostatic pressure[3]. The surrounding rock is dolomite and rock burst occurs frequently during excavation. Based on these parameters, a mechanical model is established with a size of 60 m×60 m, a buried depth of 610 m and a hydrostatic pressure of 16.84 MPa. Before excavation, the model is divided into 10429 quadrilateral elements. The grids near the cavity is locally refined. Transmission boundary conditions are applied around the model. The calculation is carried out under the conditions of plane strain and large deformation.

Physical and mechanical parameters are chosen as follows: the areal density is 2 760 kg/m²; the elastic modulus is 30 GPa; the Poisson's ratio is 0.25; σ_t is 3 MPa; the cohesion is 7.75 MPa; and φ is 34°. The type Ⅰ fracture energy is 20 N/m; the type Ⅱ fracture energy is 100 N/m; the local adaptive damping coefficient is 0.2; the friction coefficient is 0.1; the normal contact stiffness is 200 GPa; the time step is set as 1.285 84× 10^{-5} s, and the gravitational acceleration is 9.8 m/s².

The calculation procedure is similar to that presented in Section 4.2. The cavern with a diameter of 10 m is excavated from the center of the model. The cavern is excavated four times successively, corresponding to the elements with a radius of 1.25, 2.50, 3.75 and 5.00 m being deleted in turn, and the excavation interval is 500 time steps.

5.2 Model results analysis

Figure 13 depicts the spatial and temporal distribution of the fractures and σ_1 in the surrounding rock. The white and black line represent tensile fracture sections and shear fracture sections, respectively. It can be found that with the increase of the number of time steps, shear fractures appear at four symmetrical positions with 45° between the horizontal and vertical directions accompanied by the presence of some tensile fractures. The shear cracks develop into 4 V-shaped notches gradually, and there is a stress (σ_1) concentration at the tips of shear cracks. After that, the cracking behaviour of surrounding rock keeps stable. The above results are basically consistent with field observation results[3].

(a) Number of time step =5 000   (b) Number of time step =6 000

(c) Number of time step =10 000   (d) Number of time step =15 000
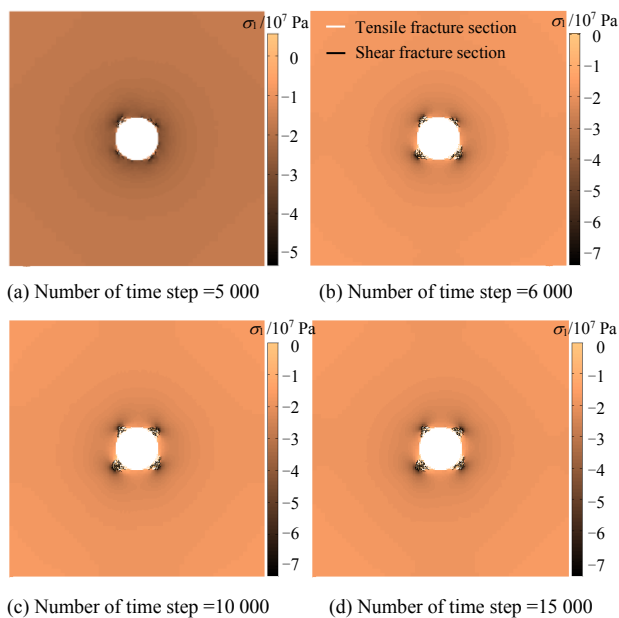
Fig. 13 Spatiotemporal distributions of cracks and σ_1 of the surrounding rock

6 Conclusions

For Brazilian disc rock specimen, tensile cracks propagate from the center of the disc to the top and bottom until they penetrate through the disc, and the tensile cracks are relatively smooth; for uniaxial compression rock specimen, shear cracks are relatively straight, and the direction of the main shear crack penetrating through the rock specimen is consistent with the shear plane direction obtained according to the Mohr-Coulomb criteria.

From the effects of hydrostatic pressure and internal friction angle on the deformation-cracking processes, the following results are found. Under hydrostatic pressure, V-shaped notches appear near the cavern surface due to shear crack propagation; then, long and curved shear cracks appear due to further shear cracks propagation whose distribution is similar to shear slip-lines. With an increase of hydrostatic pressure, the ranges of shear cracks increase, whereas with an increase of internal friction angle, the ranges of shear cracks decrease, and the angle between the propagation direction of the narrow shear cracks and the annular direction decreases, so as to the space between the adjacent shear cracks.

According to the simulation of the surrounding rock in Tianshengqiao Hydropower Station Ⅱ section 5+ 470−500, four V-shaped notches are observed, which is in a good agreement with field observations.

References

[1] HOEK E, MARTIN C D. Fracture initiation and propagation in intact rock—a review[J]. Journal of Rock Mechanics and Geotechnical Engineering, 2014, 6(4): 287−300.

[2] GONG Feng-qiang, LUO Yong, SI Xue-feng, et al. Experimental modelling on rockburst in deep hard rock circular tunnels[J]. Chinese Journal of Rock Mechanics and Engineering, 2017, 36(7): 1634−1648.

[3] LU Jia-you, WANG Chang-ming. Study on back analysis for stress of rock mass from information of rockbursts[J]. Journal of Yangtze River Scientific Research Institute, 1994, 11(3): 27−30.

[4] GUENOT A. Borehole breakout and stress fields[J]. International Journal of Rock Mechanics and Mining Sciences, 1989, 26(3−4): 185−195.

[5] CROOK T, WILLSON S, YU J G, et al. Computational modelling of the localized deformation associated with borehole breakout in quasi-brittle materials[J]. Journal of Petroleum Science & Engineering, 2003, 38(3): 177−186.

[6] CHEN Xu-guang. Study on forming mechanism and anchorage character of zonal disintegration in rock mass of deep tunnel under high geostress[D]. Jinan: Shandong University, 2011.

[7] CHANYSHEV A I. Phenomenon of zonal disintegration and plastic deformation of the deep surrounding rock[C]// Effects of Zonal Disintegration of the Surrounding Rock in Rock Engineering at Depth. Beijing: China Science and Technology Press, 2008.

[8] ZHANG Wen-ju, LU Wen-bo, YANG Jian-hua, et al. Cracking characteristics and influential factors of surrounding rocks induced by excavation unloading in deep tunnel[J]. Rock and Soil Mechanics, 2013, 34(9): 2690−2698.

[9] ZHANG Chu-han, JIN Feng, HOU Yan-li, et al. Discrete-contact-fracture analysis of rock and concrete[M]. Beijing: Tsinghua University Press, 2008.

[10] YAN C Z, ZHENG H, SUN G H, et al. Combined finite discrete element method for simulation of hydraulic fracturing[J]. Rock Mechanics and Rock Engineering, 2016, 49(4): 1389−1410.

[11] GUO Xiang, WANG Xue-bin, BAI Xue-yuan, et al. Numerical simulation of effects of loading types and tensile strengths on Brazilian disk test by use of a continuum-discontinuum method[J]. Rock and Soil Mechanics, 2017, 38(1): 214−220.

[12] LISJAK A, FIGI D, GRASSELLI G. Fracture development around deep underground excavations: insights from FDEM modeling[J]. Journal of Rock Mechanics and Geotechnical Engineering, 2014, 6(6): 493−505.

[13] YAN Cheng-zeng, SUN Guan-hua, ZHENG Hong, et al. Adaptive FEM/DEM analysis method based on the local splitting elements[J]. Rock and Soil Mechanics, 2014, 35(7): 2064−2070.

[14] YAN Cheng-zeng, ZHENG Hong, GE Xiu-run. Unified calibration based potential contact force in discrete element method[J]. Rock and Soil Mechanics, 2015, 36(1): 249−256.

[15] LISJAK A, TATONE B S A, MAHABADI O, et al. Hybrid finite-discrete element simulation of the EDZ formation and mechanical sealing process around a microtunnel in Opalinus clay[J]. Rock Mechanics and Rock Engineering, 2016, 49(5): 1849−1873.

[16] LIU Quan-sheng, DENG Peng-hai, BI Chen, et al. FDEM numerical simulation of the fracture and extraction process of soft surrounding rock mass and its rockbolt-shotcrete-grouting reinforcement methods in the deep tunnel[J]. Rock and Soil Mechanics, 2019, 40(10): 4065−4083.

[17] WANG Xue-bin, MA Bing, PAN Yi-shan, et al. Numerical simulation of the stress wave propagation and collapsing process of the tunnel surrounding rock[J]. Journal of China University of Mining & Technology, 2017, 46(6): 1259−1266.

[18] MUNJIZA A. The combined finite-discrete element method[M]. London: John Wiley and Sons, 2004.

[19] LISJAK A, TATONE B S A, GRASSELLI G, et al. Numerical modelling of the anisotropic mechanical behaviour of Opalinus clay at the laboratory-scale using FEM/DEM[J]. Rock Mechanics and Rock Engineering, 2014, 47(1): 187−206.

[20] ZHAO Yi-xin, LIU Bin, YANG Zhi-liang, et al. Tensile strength and fracture toughness of sedimentary rocks at different buried depths in Shendong coal field[J]. Journal of China Coal Society, 2019, 44(6): 1732−1741.